Supplementary Information for

Unveiling inherent functions of rock-salt phase character and multi-dimensional structural engineering of NiCoO$_2$ anode for high-power and long-life lithium ion batteries

Sheng Chen[a], Wei Wei[a],*, Tianyi Ding[a], Yunping Wu[a], Rui Zhai[a], Caihe Bai[a] and Fei Wang[b]

[a] *Department of Applied Chemistry, School of Chemistry, Xi'an Key Laboratory of Sustainable Energy Material Chemistry, Xi'an Jiaotong University, Xi'an 710049, P. R. China*
[b] *School of Chemistry and Materials Science, Huaibei Normal University, Huaibei 235000, P. R. China*

*E-mail: wwei.mc@mail.xjtu.edu.cn

Experimental section

Materials synthesis

Synthesis of flower-like Ni/Co-glycolate microspheres precursor: All chemicals were used as received without further purification. Typically, 0.22 g $Ni(NO_3)_2 \cdot 6H_2O$ and 0.22 g $Co(NO_3)_2 \cdot 6H_2O$ were dissolved into a mixture of 45 mL isopropanol, 30 mL glycol, and 1.5 mL deionized water under magnetic stirring. The mixture was kept stirring for 30 min at room temperature, then transferred into a 100 mL Teflon-lined autoclave for solvothermal reaction at 180°C for 12h. After being naturally cooled down to room temperature, the light pink precipitates were collected via centrifugation, washed with deionized water several times, and dried at 80 °C overnight.

Preparation of NCO@NC-FMS composites: Firstly, 200 mg of the as-prepared precursor was dispersed in 100 mL Tris-buffer (pH =8.5) by ultrasound for 20 min, then 100 mg dopamine (DA) hydrochloride was added into the mixture (1 mg mL^{-1}) to start the polymerization under magnetic stirring at room temperature for 24h. The obtained black precipitates were collected by vacuum filtration and washing, then dried at 80°C overnight. Subsequently, the Ni/Co-glycolate@PDA intermediate was sintered and carbonized at 450 °C for 3h with a ramp rate of 2 °C min^{-1} under Ar, giving rise to NCO@NC-FMS composites.

Preparation of NCO-FMS, NCO@NC and $NiCo_2O_4$@NC-FMS: For comparison, flower-like NCO microspheres (NCO-FMS) without NC coating were prepared by directly annealing the glycolate precursor. For NCO@NC composites, bulk NCO precursor was firstly prepared using similar solvothermal method in mixed solvents of isopropanol and glycol (in the absence of water), and the following procedures were the same to that of NCO@NC-FMS. For the $NiCo_2O_4$@NC-FMS, flower-like $NiCo_2O_4$ precursor were firstly prepared using the similar solvothermal process by changing the mole ratio of nickel/cobalt salts to 0.5. The resultant precursor was then sintered at 450 °C in air to obtain $NiCo_2O_4$-FMS. After same coating by PDA layers, the intermediate was calcined at 300 °C for 5h under Ar to generate $NiCo_2O_4$@NC-FMS.

Material characterizations

The crystal structures were identified by X-ray diffraction (XRD, Bruker D8 advancer) with Cu Kα radiation (λ= 0.15418 nm). Raman spectra were obtained using a laser of 532 nm by Raman microscope (LabRAM HR 800). Carbon content was measured by thermo-gravimetric analysis with a TGA2 system (SF1100, China) at a ramping rate of 10°C min^{-1} in air. X-ray photoelectron spectroscopy (XPS) spectra were performed on Thermo Fisher ESCALAB Xi+ X-ray photoelectron spectrometer. The morphologies were characterized by field-emission scanning electron microscopes (FESEM, GeminiSEM 500 and JSM-7000F) equipped with energy-dispersive X-ray spectroscopy (EDX). The microstructures were characterized by a transmission electron microscope (TEM, JEM-2100). Nitrogen adsorption-desorption isotherms and pore characteristics were measured on a Micrometrics ASAP 2020.

Electrochemical measurement

To fabricate the anodes, the prepared active materials were mixed with carbon

black (Super-P) and polyvinylidene fluoride (PVDF) (7:2:1) in N-methyl-2-pyrrolidone (NMP). The resultant slurry was coated onto Cu foils and dried at 60 °C in vacuum overnight. The electrode slices were then cut into disks with diameter of 1.2 cm. CR-2016 type coin cells were assembled in a glove box under high-purity argon, using above working electrodes, lithium foil as counter electrodes and Celgard 2400 membranes as separator. The electrolyte was 1.0 M $LiPF_6$ dissolved in the mixed solvent of ethylene carbonate (EC) and dimethyl carbonate (DMC) (1:1 in volume). The mass loading of the active materials was around 1 mg cm^{-2}. The electrochemical performance was evaluated using a Land CT2001A battery test system over the voltage range between 0.01–3.0 V (vs. Li/Li$^+$). Cyclic voltammetry (CV) and electrochemical impedance spectroscopy (EIS) were operated on a CHI660D electrochemical workstation. All of the measurements were carried out at room temperature.

For packaging the full cells, the positive electrode was prepared by mixing commercial $LiNi_{0.8}Co_{0.1}Mn_{0.1}O_2$ (NCM811), Super-P and PVDF with a gravimetric ratio of 8:1:1 in NMP. The resulting slurry was coated on an aluminum foil and further vacuum-dried at 110 °C. Before assembling a full cell, the NCO@NC-FMS anodic electrode was pre-lithiated for two cycles in a half-cell to compensate the initial lithium loss. The full devices were assembled with the same procedures as those for the half cells, except applying commercial NCM811 as the positive electrode, with a designed anode/cathode capacity ratio of 1.1–1.5:1.0. Both the current density and specific capacity were calculated based on the mass of cathode. The calculation of specific energy density (E) of devices was based on the equation $E = C \times V \times (1 - \delta)$, in which V, C, and δ represent average potential, specific discharge capacity, and the penalty factor, respectively.[1]

Computational methods

The Vienna Ab initio Simulation Package (VASP) was employed to perform all the density functional theory (DFT) calculations within the generalized gradient approximation (GGA) using the PBE formulation.[2–4] The projected augmented wave (PAW) potentials were chosen to describe the ionic cores, and valence electrons were taken into account using a plane wave basis set with a kinetic energy cutoff of 500 eV.[5,6] Partial occupancies of the Kohn-Sham orbitals were allowed using the Gaussian smearing method with a width of 0.05 eV. The electronic energy was considered self-consistent as the energy change was smaller than 10^{-5} eV. A geometry optimization was considered convergent when the force change was smaller than 0.04 eV/Å. Grimme's DFT-D3 methodology was used to describe the dispersion interactions.[7]

The equilibrium lattice constants of $NiCoO_2$ and $NiCo_2O_4$ unit cells were optimized using a 8×8×6 Monkhorst-Pack k-point grid for Brillouin zone sampling. We had further used the supercell method to eliminate the problem of fractional occupancy. Then, supercell models with 2×2×2 periodicity for $NiCoO_2$ and 1×1×1 periodicity for $NiCo_2O_4$ structure had been constructed in the x, y and z directions. The 3×3×2 Monkhorst-Pack k-point grid for Brillouin zone was used for k-point sampling during structural optimizations and all atoms were allowed to relax. Finally, each free energy had been calculated and the U correction had been set as 3.68 eV and 3.85 eV for Co and Ni atoms in our systems. The unit structures of reactants and

products were constructed by referring to the materials project database, and the amorphous Li_2O structure was calculated using Ab Initio molecular dynamics (AIMD). In our work, the free energies (G) of all species cells were computed from corresponding supercell and divided by their coefficients in the lithiation reactions. Then, the free energies per cell (G/ unit cell) were obtained by $G = E_{total} + E_{ZPE} - TS$, where E_{total}, E_{ZPE}, and TS are the ground-state energy per unit cell, zero-point energies, and entropy terms with 300K, respectively. The E_{ZPE} and TS were taken vibration frequencies from DFT. Finally, the energy difference (ΔG) of reaction is defined as $\Delta G = G_{products} - G_{reactants}$.
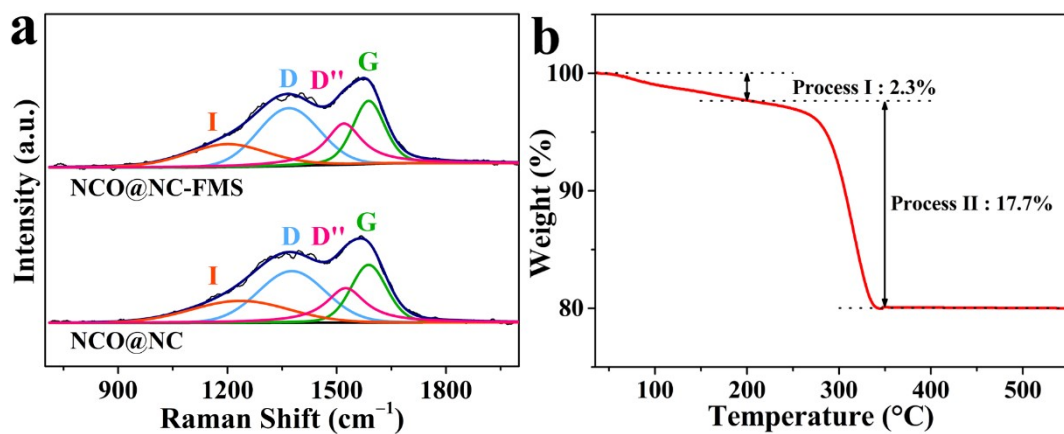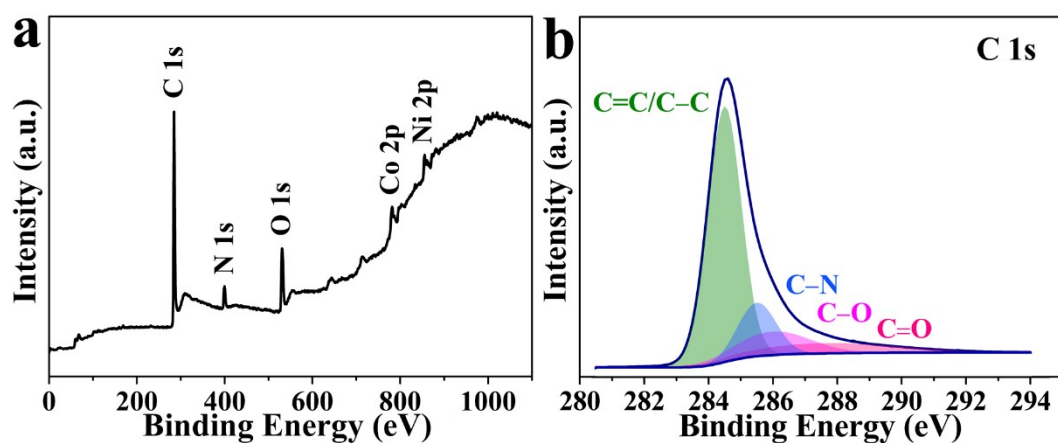
Figures
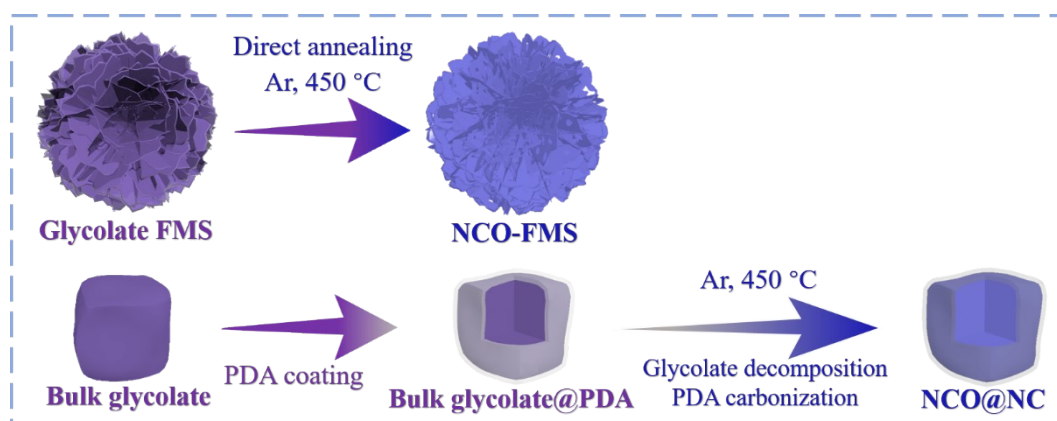
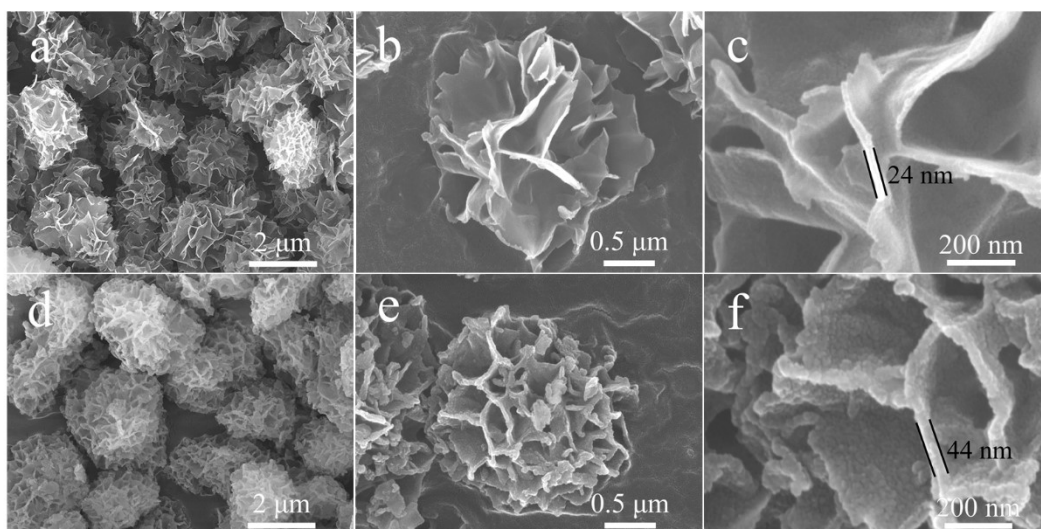**Fig. S1** Schematic illustration for the fabrication of NCO-FMS and NCO@NC.
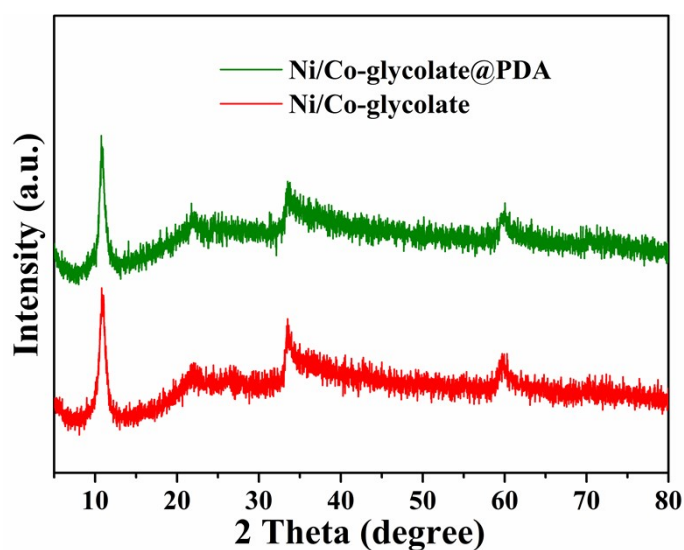
**Fig. S2** XRD patterns of the Ni/Co-glycolate precursor and glycolate@PDA intermediate.

Fig. S3 (a) The fitted Raman spectra of NCO@NC-FMS and NCO@NC. (b) TG curve of the NCO@NC-FMS product.
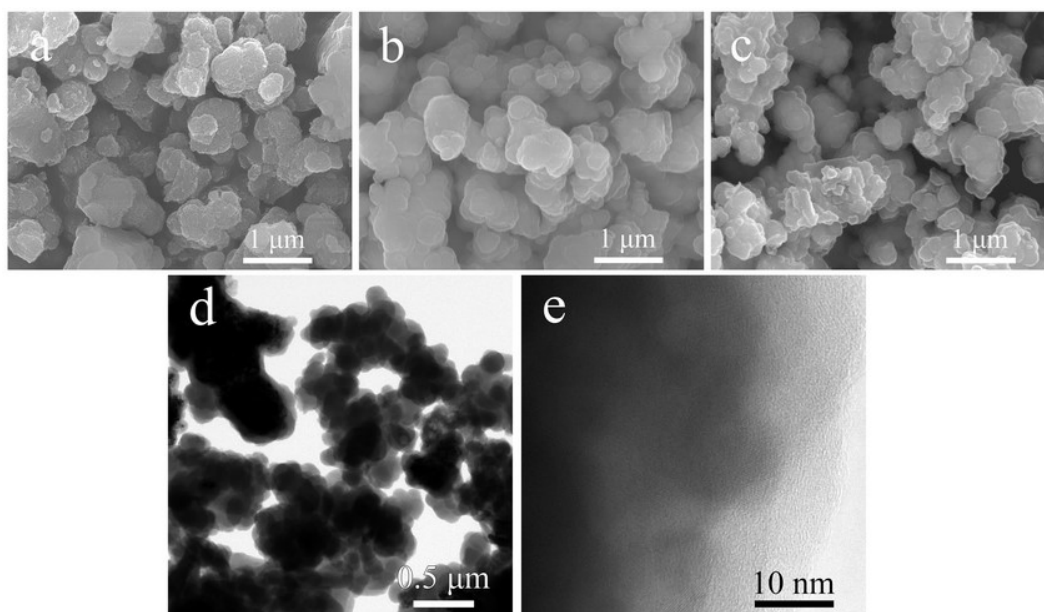

Fig. S4 (a) XPS survey spectrum of the NCO@NC-FMS. (b) High resolution XPS spectrum of the C 1s.
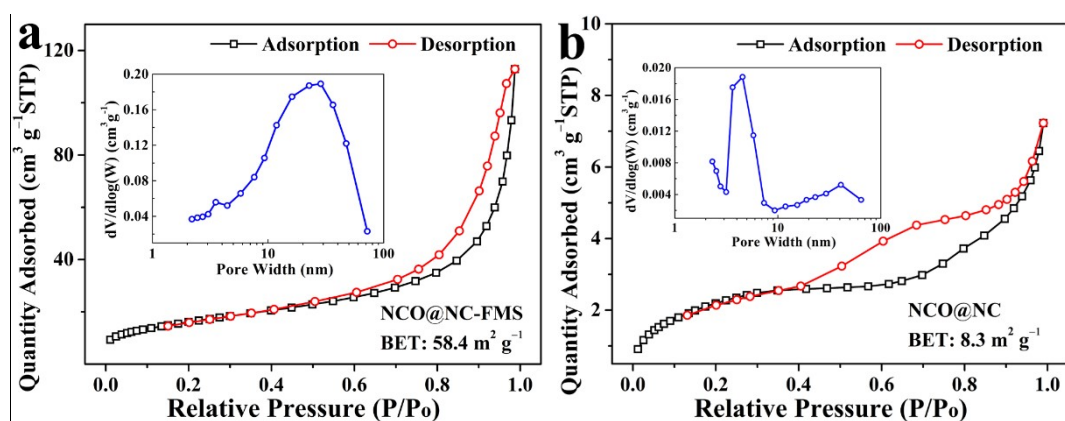
Fig. S5 FESEM images at different magnifications of: (a–c) Ni/Co-glycolate FMS precursors, (d–f) glycolate@PDA FMS intermediates.
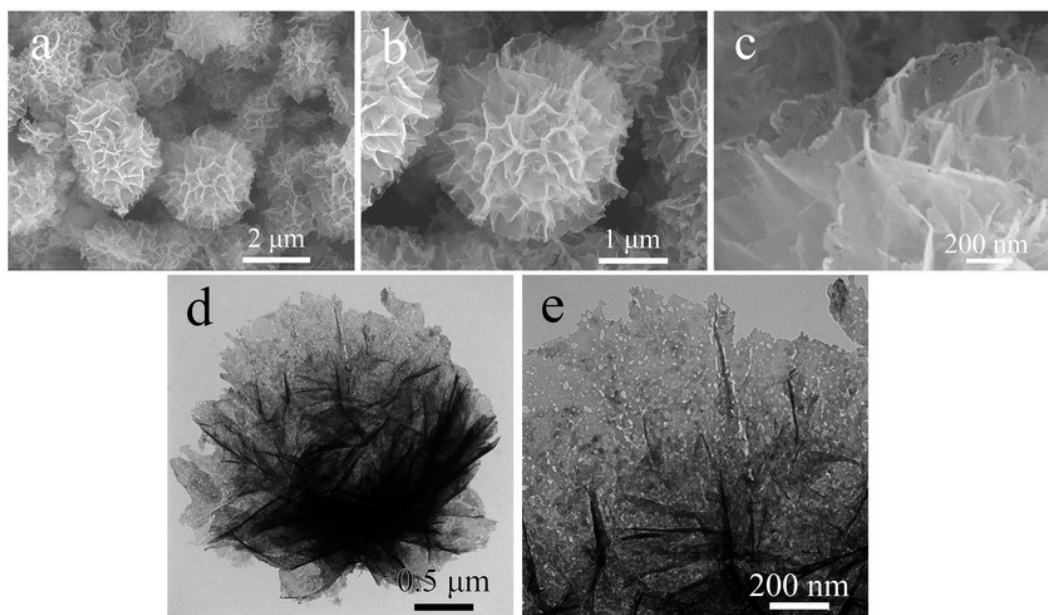
Fig. S6 (a–c) FESEM and (d–e) TEM images at different magnifications of NCO-FMS.

Fig. S7 FESEM images: (a) Bulk Ni/Co-glycolate, (b) bulk glycolate@PDA and (c) NCO@NC. (d–e) TEM images of NCO@NC.


Fig. S8 Nitrogen adsorption-desorption isotherms and corresponding BJH pore-size-distribution (inset) of (a) NCO@NC-FMS and (b) NCO@NC.

The hysteresis loops appearing at the P/P_0 of 0.4–0.98 indicate the presence of mesopores.[8] The total pore volume and average pore diameter of NCO@NC-FMS are 0.17 cm^3 g^{-1} and 11.95 nm, larger than those of NCO@NC (0.01 cm^3 g^{-1} and 5.39 nm).
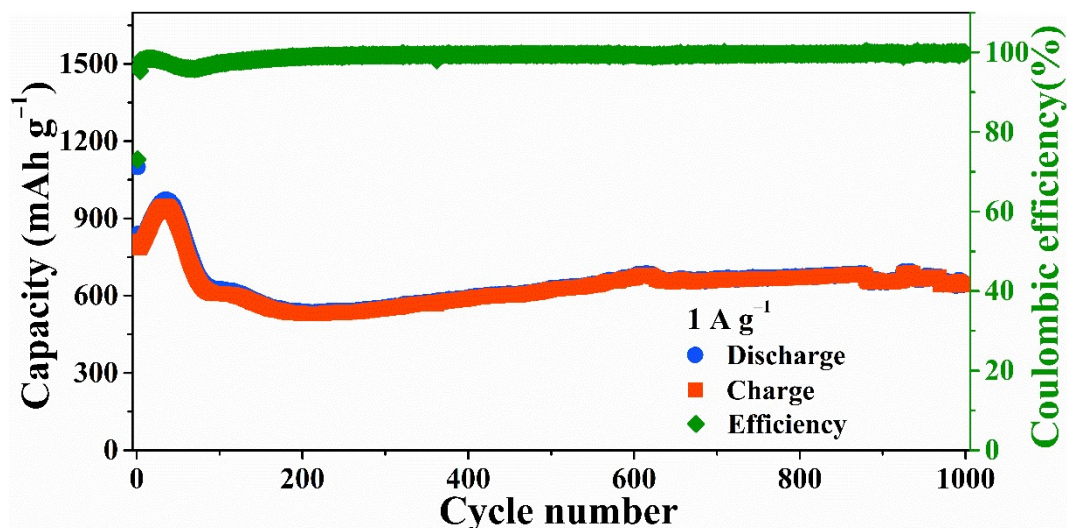
Fig. S9 Long-term cycling stability of NCO@NC-FMS at 1 A g^{-1}.

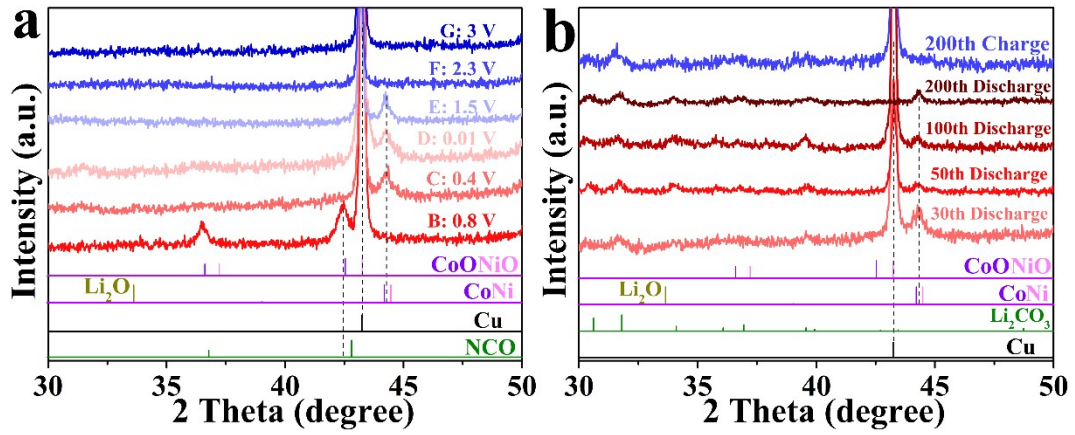|	R_f	R_{ct}
NCO@NC-FMS	104	76
NCO@NC	165	295
NCO-FMS	235	315
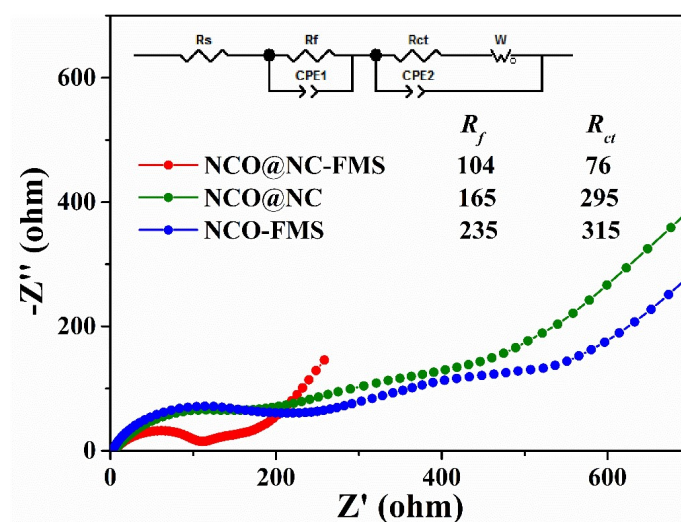
Fig. S10 The Nyquist plots with corresponding value of R_f and R_{ct} of NCO@NC-FMS, NCO@NC and NCO-FMS after 400 cycles, the inset picture is an equivalent circuit.
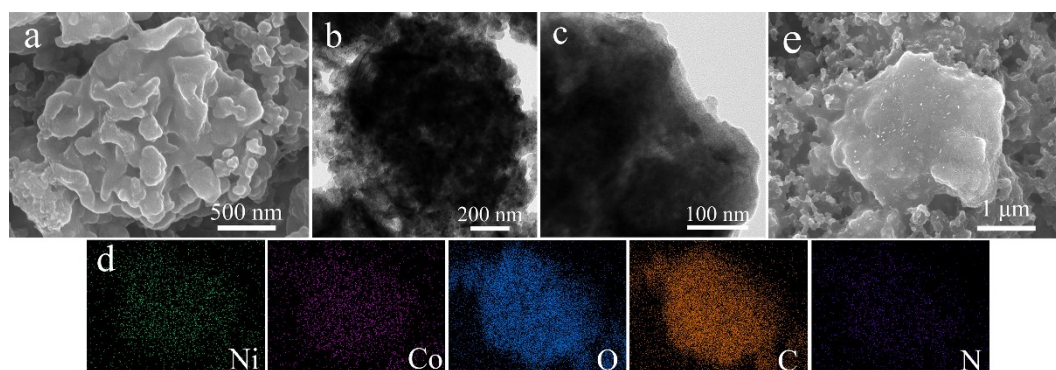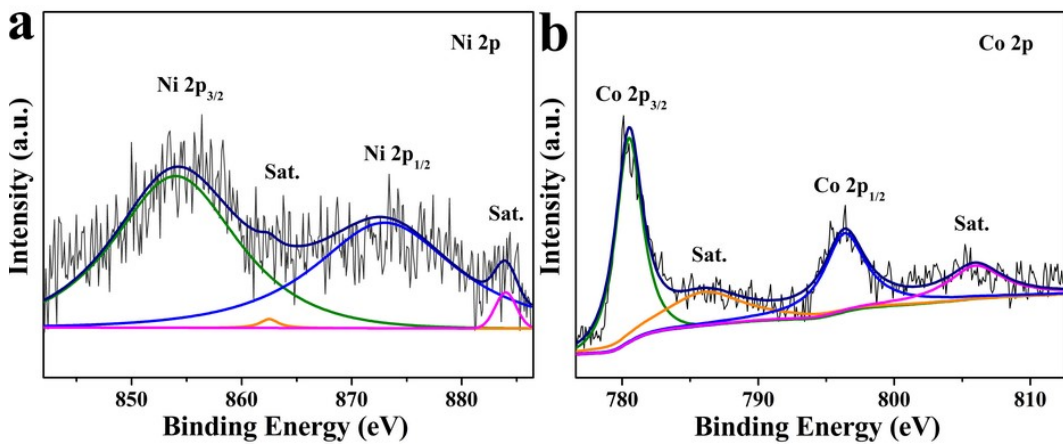

Fig. S11 (a) FESEM, (b, c) TEM, and (d) EDX elemental mapping images of the cycled NCO@NC-FMS anode material. (e) FESEM images of the cycled NCO-FMS anode.
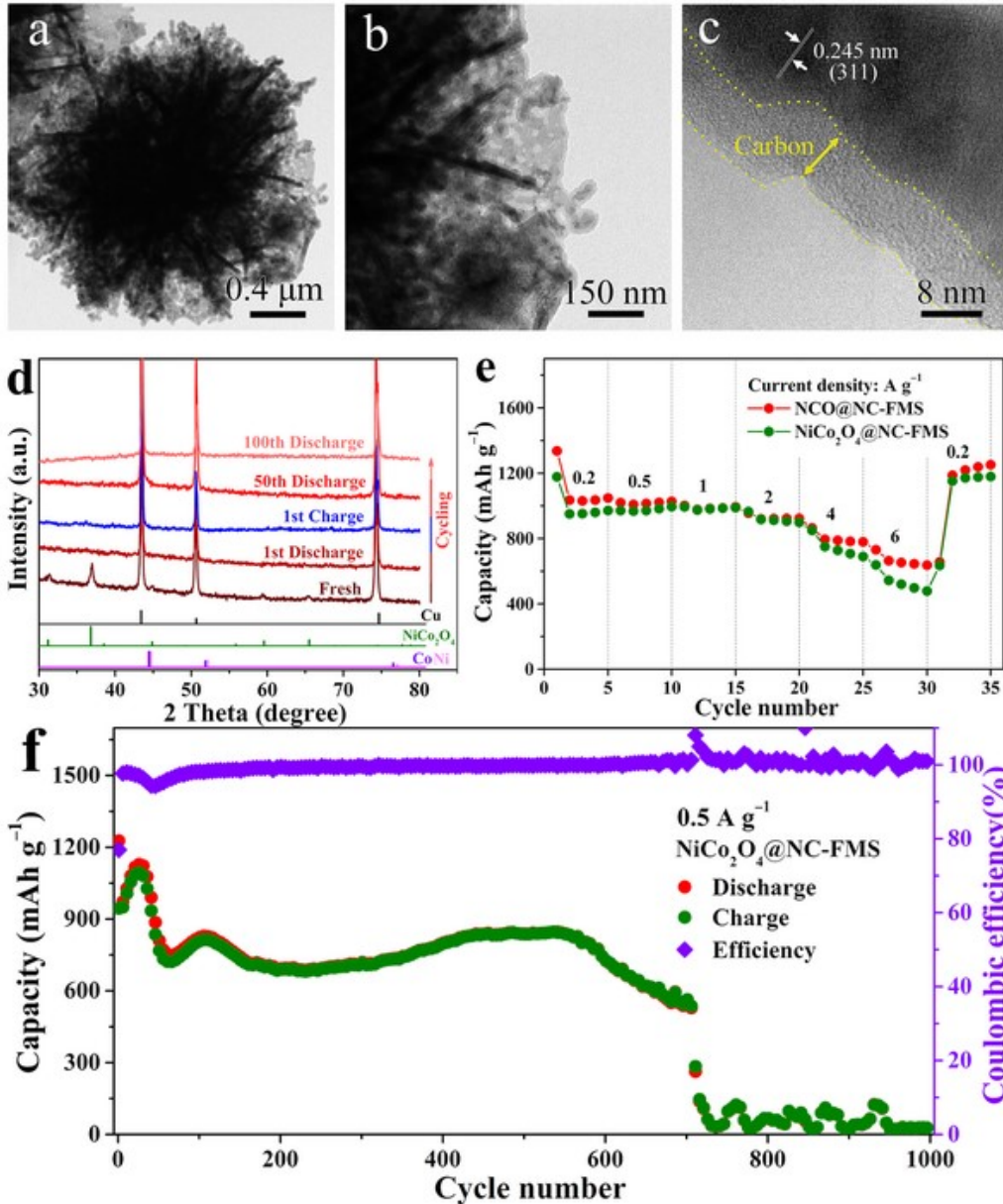
Fig. S12 Enlarged e*x-situ* XRD patterns of electrodes: (a) at different stages during the first cycle (200 mA g^{-1}) and (b) after fully discharge or charge in specific cycles.

Fig. S13 XPS spectra of the NCO@NC-FMS electrode after 1st charge: (a) Ni2p, (b) Co 2p.

Fig. S14 Morphology characterizations and electrochemical performance of NiCo$_2$O$_4$@NC-FMS: (a–c) TEM images at different magnifications. (d) *Ex-situ* XRD patterns obtained at a fresh state and fully discharge or charge stages after the specific cycles. (e) Rate behaviors in comparison with NCO@NC-FMS. (f) Long-term cycling performance at 0.5 A g^{-1}.
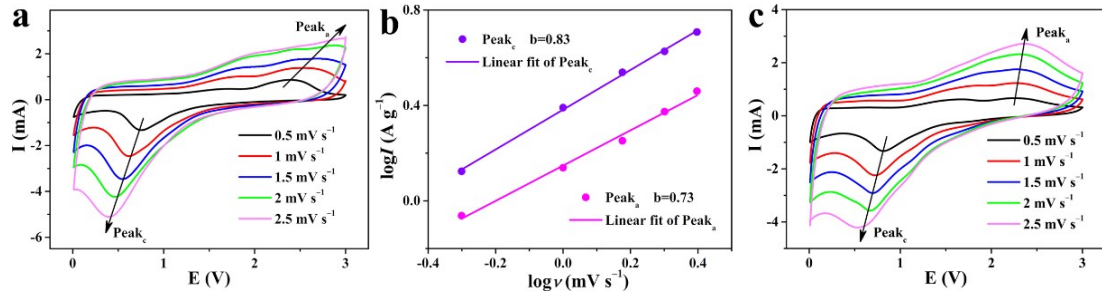
Fig. S15 (a) CV curves and (b) corresponding relationship between log i and log v of NCO@NC-FMS. (c) CV curves of NiCo$_2$O$_4$@NC-FMS.

Further kinetic analysis of NCO@NC-FMS and NiCo$_2$O$_4$@NC-FMS were performed based on the CV measurements ranging from 0.5 to 2.5 mV s^{-1} (Fig. S15a). The scan rate v and peak current i obey equations:[9,10]

$$i = av^b \tag{1}$$

$$\log i = \log a + b \log v \tag{2}$$

where a and b are adjustable values, b can be calculated from the slope of fitting linear between log i versus log v. In the case of 0.5<b<1.0, the total charge storage behavior can be divided into two separate components: the Li$^+$ diffusion controlled behavior and surface-induced pseudo-capacitance process. As fitted in Fig. S15b, the b value of NCO@NC-FMS for the anodic and cathodic peaks were calculated as 0.73 and 0.83, respectively, which indicate partial pseudo-capacitive behavior exists in NCO@NC-FMS. The corresponding proportions can be determined by the evaluation of current response (i) at the fixed potential (v) at various sweep rates based on the following equation:[11,12]

$$i = k_1 v + k_2 v^{1/2} \tag{3}$$

where i is the response current at the potential of v, and k_1v and $k_2v^{1/2}$ are the current contributions from the capacitive and diffusion-controlled processes, respectively. k_1 and k_2 can be determined from the relationship between i(v)/v and i(v)/$v^{1/2}$.

Fig. S16 The photograph on tap density measurement of NCO@NC-FMS.

The tap density was measured by vibrating the glass cylinder until the height of the NCO@NC-FMS sample did not fall off. The ratio of the mass and the volume determines the tap density of the sample.
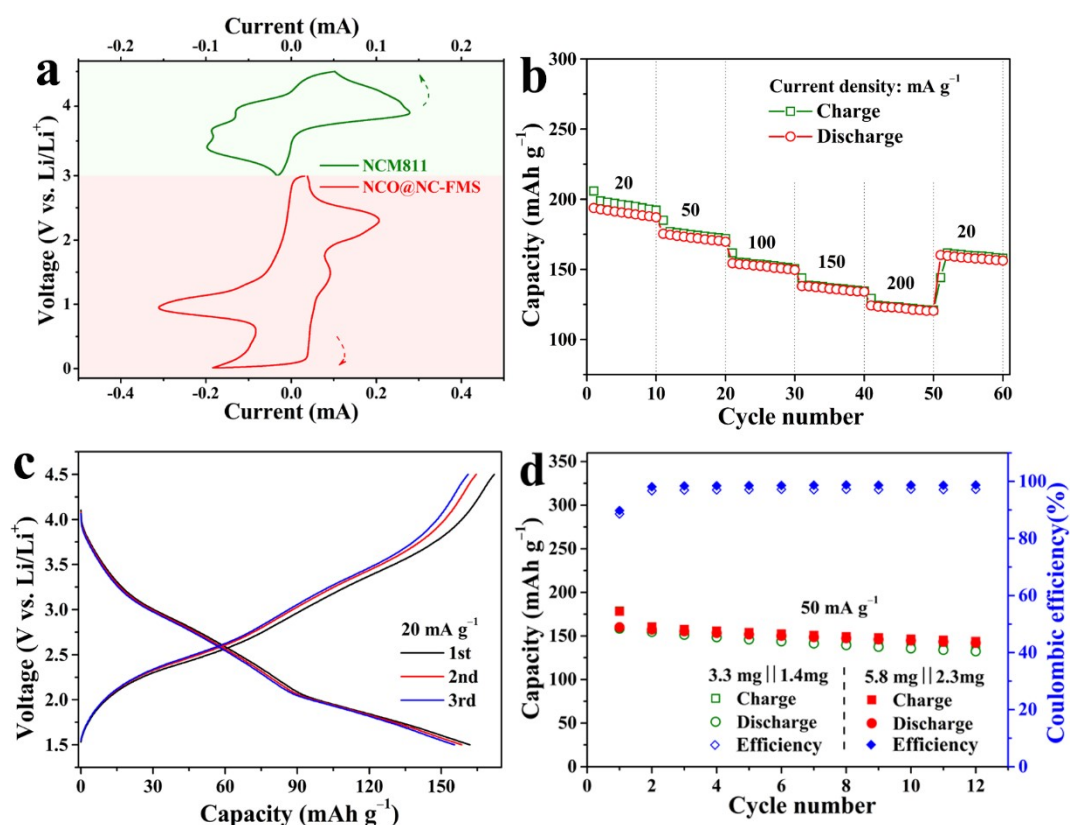
Fig. S17 (a) CV curves (0.1 mV s^{-1}) of the NCM811 (green color) and NCO@NC-FMS (red color) electrodes in half cells. (b) Rate performance of the NCM811 positive electrode in a half cell. (c) Charge-discharge curves of the as-prepared full cell for the first three cycles at 20 mA g^{-1}. (d) Electrochemical performance of full

cells after five activation cycles with higher mass amount of each electrode.

Table S1 Comparisons of the diffusion coefficients (D_{Li^+}) of NCO@NC-FMS with NiCo$_2$O$_4$@NC-FMS and other previously influential Ni-Co-O based anodes.

Samples	D		Ref.
	D_c	D_a	
NiCoO$_2$ nanoparticles embedded in flower-like carbon microspheres	2.33×10^{-8}	4.56×10^{-9}	Our work
Hollow NiCoO$_2$ sub-microspheres	6.32×10^{-8}	3.66×10^{-8}	13 J. Mater. Chem. A
Nanodimensional NiCoO$_2$ encapsulated in porous carbon submicrospheres	2.97×10^{-8}	1.08×10^{-8}	14 ACS Appl. Mater. Interfaces
Ultrafine NiCoO$_2$ nanoparticles@ultralong carbon nanofibers	2.1×10^{-9}		15 Chem. Eur. J.
NiCo$_2$O$_4$ nanoparticles embedded in flower-like carbon microspheres	2.93×10^{-9}	7.37×10^{-10}	Our work
Individually dispersed NiCo$_2$O$_4$ anchoring on checkerboard-like C/CNT nanosheets	0.28×10^{-14}		16 J. Mater. Chem. A
Surfacing Ni–B nanoflakes on NiCo$_2$O$_4$ nanospheres	2.36×10^{-10}	1.70×10^{-10}	12 Nanoscale
Conductive polypyrrole coated hollow NiCo$_2$O$_4$ microspheres	1.86×10^{-13}		17 ChemElectroChem
1D bundle-like NiCo$_2$O$_4$@TiO$_2$ hybrid	3.89×10^{-11}		18 Chem. Eng. J.
Flower-like NiCo$_2$O$_4$ tuned by graphene oxide	5.727×10^{-13}		19 Electrochim. Acta
Porous hollow superlattice NiMn$_2$O$_4$/NiCo$_2$O$_4$ mesocrystals	1.19×10^{-11}		20 Front. Chem.

References

[S1] L. Shen, S. Chen, J. Maier and Y. Yu, *Adv. Mater.*, 2017, **29**, 1701571.

[S2] G. Kresse and J. Furthmuller, *Comp. Mater. Sci.*, 1996, **6**, 15–50.

[S3] G. Kresse and J. Furthmuller, *Phys. Rev. B*, 1996, **54**, 11169–11186.

[S4] J. Perdew, K. Burke and M. Ernzerhof, *Phys. Rev. Lett.*, 1996, **77**, 1396.

[S5] G. Kresse and D. Joubert, *Phys. Rev. B*, 1998, **59**, 1758–1775.

[S6] P. Blochl, *Phys. Rev. B*, 1994, **50**, 17953–17979.

[S7] S. Grimme, J. Antony, S. Ehrlich and H. Krieg, *J. Chem. Phys.*, 2010, **132**, 154104.

[S8] M. Huang, K. Mi, J. Zhang, H. Liu, T. Yu, A. Yuan, Q. Kong and S. Xiong, *J. Mater. Chem. A*, 2017, **5**, 266–274.

[S9] Z. Zheng, P. Li, J. Huang, H. Liu, Y. Zao, Z. Hu, L. Zhang, H. Chen, M.-S. Wang, D.-L. Peng and Q. Zhang, *J. Energy Chem.*, 2020, **41**, 126–134.

[S10] P. Ge, S. Li, L. Xu, K. Zou, X. Gao, X. Cao, G. Zou, H. Hou and X. Ji, *Adv. Energy Mater.*, 2019, **9**, 1803035.

[S11] C. Zhang, Z. Xie, W. Yang, Y. Liang, D. Meng, X. He, P. Liang and Z. Zhang, *J. Power Sources*, 2020, **451**, 227761–227769.

[S12] M. Li, Q. Zhou, C. Ren, N. Shen, Q. Chen, J. Zhao, C. Guo, L. Zhang and J. Li, *Nanoscale*, 2019, **11**, 22550–22558.

[S13] Z. Wang, D.K. Denis, Z. Zhao, X. Sun, J. Zhang, L. Hou and C. Yuan, *J. Mater. Chem. A*, 2019, **7**, 18109–18117.

[S14] D.K. Denis, Z. Wang, X. Sun, F.U. Zaman, J. Zhang, L. Hou, J. Li and C. Yuan, *ACS Appl. Mater. Interfaces*, 2019, **11**, 32052–32061.

[S15] Z. Wang, Z. Zhao, Y. Zhang, X. Yang, X. Sun, J. Zhang, L. Hou and C. Yuan, *Chem. Eur. J.*, 2019, **25**, 863–873.

[S16] H. Wang, L. Hu, C. Wang, Q. Sun, H. Li and T. Zhai, *J. Mater. Chem. A*, 2019, **7**, 3632–3641.

[S17] Y. Luo, R. Guo, T. Li, F. Li, L. Meng, Z. Yang, Y. Wan and H. Luo, *ChemElectroChem*, 2018, **6**, 690–699.

[S18] P. Liu, Q. Ru, Z. Wang, B. Wang, Q. Guo, P. Zhang, X. Hou, S. Su and F.C.-C. Ling, *Chem. Eng. J.*, 2018, **350**, 902–910.

[S19] Q. Gan, B. Liu, K. Zhao, Z. He and S. Liu, *Electrochim. Acta*, 2018, **279**, 152–160.

[S20] L. Li, Q. Yao, J. Liu, K. Ye, B. Liu, Z. Liu, H. Yang, Z. Chen, J. Duan and B. Zhang, *Front. Chem.*, 2018, **6**, 153–163.